JOURNAL OF MATERIALS SCIENCE **35** (2000) 2815–2824

Alumina-mullite-zirconia composites obtained by reaction sintering

Part II *R-Curve behavior*

A. C. MAZZEI, J. A. RODRIGUES, V. C. PANDOLFELLI
Department of Materials Engineering, Universidade Federal de São Carlos, São Carlos, S.P., Brazil
E-mail: josear@power.ufscar.br

Applying Linear Elastic Fracture Mechanics equations and sample compliance variation to quantify the instantaneous crack length, the *R*-curve behavior of alumina-mullite-zirconia composites obtained by reaction sintering, was evaluated as a function of zirconia and mullite content. Changes in the *R*-curve profile as a function of the notch geometry (Chevron and straight-through notch) was observed and discussed, based on the analysis of the $y(\alpha)$ function applied to each notch type. The influence of the $y(\alpha)$ function in the *R*-curve shape was observed in both the initial and the final crack propagation region where, in the latter, the *R*-curves presented a sharp increase. In order to suppress these effects, the *R*-curve values for pure alumina were deducted from those obtained for the different composites produced. The analysis of the resulting curves highlights the influence of the amount of zirconia and mullite inclusions in these composites.

1. Introduction

Strengthening of ceramic materials by zirconia particles is widely known. Depending on processing conditions, zirconia particle size, the presence of stabilizing oxides (i.e. CaO, MgO, Y_2O_3 or CeO_2), the volumetric fraction of zirconia in the composite [1], among other factors, a toughening mechanism known as stress-induced phase transformation can occur. Changes in the above listed parameters may generate microcracks in the matrix, which can also dissipate the crack propagation energy [1, 2] by crack branching. Therefore, improving the mechanical properties of ceramic materials containing zirconia particles is feasible [3], although the price of high quality zirconia powders renders the benefits costly.

For alumina based ceramics, composites can be produced using zircon rather than zirconia as the initial precursor. A dissociative reaction of the zircon provides zirconia and silica. This free silica reacts with alumina, producing mullite in a process known as reaction sintering [4]. Depending on the amount of reactants (alumina and zircon), a mullite-zirconia composite (mullitic matrix with zirconia inclusions) [5] or an alumina-mullite-zirconia one (alumina matrix with mullite and zirconia inclusions) is obtained. In the latter, it is possible to associate toughening mechanisms provided by the zirconia inclusions, as well as those related to the presence of the needle-like mullite. Furthermore, the addition of mullite in an alumina matrix offers additional benefits due to its high refractoriness and lower thermal expansion coefficient.

An *R*-curve represents the crack growth resistance or the resistance to the creation of a new fracture surface as a function of the instantaneous crack length. Some examples of *R*-curves are given in Fig. 1, which contains a schematic illustration of three different types of curves. The flat *R*-curve is obtained for perfectly brittle linear elastic materials that are incapable of affording any further mechanisms that dissipate the crack propagation energy. Glasses and most fine grain size ceramics, such as alumina, SiC and Si_3N_4 present this behavior, where the *R*-values are independent of the crack length [6].

Fig. 1 also shows two other different types of rising *R*-curves. The curve with an initial growth followed by a plateau, illustrates a toughening mechanism that displays a wake zone of constant size (i.e. stress induced phase transformation and bridging). The second rising *R*-curve model in Fig. 1 exemplifies cases where the wake zone extends indefinitely (i.e. crack branching). When a specific toughening mechanism is prevails, a particular *R*-curve profile is expected, in line with that mechanism. It is, therefore, possible to infer the toughening mechanisms by analyzing the shape of the *R*-curve.

Unfortunately, the relationship between the shape of the *R*-curve and the toughening mechanism is not always so straightforward, since the *R*-curve shape is also affected by testing parameters. In order to obtain an *R*-curve profile it is necessary to produce samples having specific dimensions and geometry, to obtain a load versus displacement curve ($P \times \delta$-curve) under a stable crack propagation condition, and to work out the

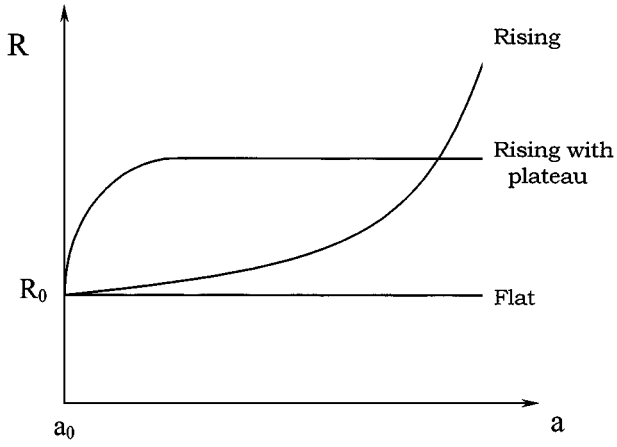

Figure 1 Schematic drawing of three different types of *R*-curves: rising, rising with plateau, and flat. *R* is the crack resistance, R_0 its initial value, a_0 is the initial crack length and *a* its instantaneous length.

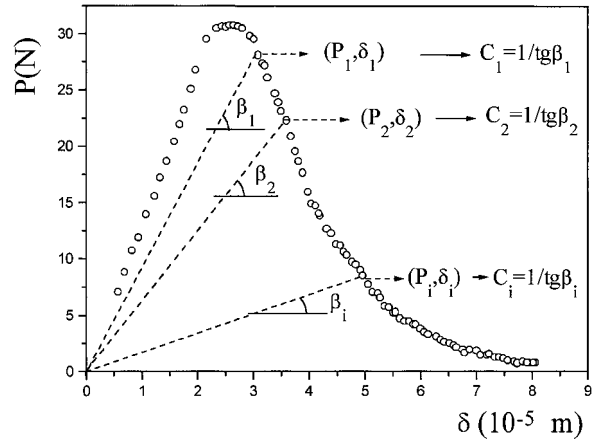

Figure 2 Procedure used to evaluate the experimental relation between the compliance (C_i) and the instantaneous crack length (a_i). The figure displays a typical $P \times \delta$ stable crack propagation curve. The (P_i, δ_i) points are used to work out the experimental compliance, $C_i = 1/tg\beta_i$.

values of the instantaneous crack length leading to the *R*-values.

The geometry and dimensions of samples are chosen according to the microstructural characteristics of the material and the experimental fixtures used to obtain the $P \times \delta$-curve. For brittle materials, Chevron notched samples are recommended since this notch shape helps stable crack propagation. For flexural tests, it is also important to reduce the dimensions of the sample as long as the crack extension limit exceeds fifty times the average grain size [7].

Regarding determination of the instantaneous crack length, Table I presents some of the possibilities to work it out.

There are several different testing modes to obtain a sample *R*-curve. The precise relation between the *R*-curve shape and the toughening mechanisms requires a comprehensive knowledge of the influence of each test parameter on the *R*-curve shape. Based on this perspective, this study evaluates the variation of the *R*-curve shape for different notches and testing geometry, as well as the influence of the $y(\alpha)$ function for alumina-mullite-zirconia composites. The sample dimensions and methodologies applied to calculate instantaneous crack length as well as the *R*-curve were kept constant.

TABLE I Possible tests and methodologies to obtain an experimental *R*-curve

Determination of the instantaneous crack length	Test([a])	Calculation of the *R*-values
Compliance change	1. Continuous loading	1. LEFM (linear elastic fracture mechanics)
	2. Loading-unloading	
	3. CMOD and continuous loading	
	4. CMOD and loading-unloading	2. Energetic method
Direct observation	1. Continuous loading	1. LEFM
		2. Energetic method
CMOD (Crack Mouth Opening Displacement)	1. Loading-unloading	1. Fracture mechanics of two parameters [8, 9].

[a]The test geometry (i.e., flexural test under three or four-point bending) as well as the notch geometry (i.e., Chevron and straight-through notches) can also be elected.

1.1. *R*-curve calculation method

The flexural test was selected for this work due to its simple requirements for the preparation of samples. The samples were Chevron or straight-through notched. A low displacement rate was used (1 μm/min) to obtain stable crack propagation.

The instantaneous crack length, *a*, was indirectly obtained by the change in compliance, *C* [10]. Assuming the linear elastic behavior, straight lines were drawn from the origin up to different (P_i, δ_i) intersections of the $P \times \delta$-curves obtained under stable crack propagation conditions (Fig. 2). The slope of these lines, given by $tg(\beta_i) = P_i/\delta_i$, defines the instantaneous stiffness of the sample which, in turn, is the reciprocal of the instantaneous compliance, C_i. Applying this technique for the samples' $P \times \delta$-curves the *experimental compliance values*, $C_i(a_i)$ were obtained. The instantaneous crack length, a_i, was calculated comparing the values of $C_i(a_i)$ with those obtained theoretically. An iterative fitting method was used to make this comparison.

The following statements were taken into account [11] to obtain the *theoretical compliance values*. Considering the samples' dimensions shown in Fig. 3, and defining Young's Modulus as *E*, it follows that:

$$G = \frac{K_I^2}{E} = \left(\frac{P^2}{2b}\right) \cdot \frac{dC}{da} = R, \qquad (1)$$

where *G* is the elastic energy release rate, K_I is the stress intensity factor at the crack tip, *P* is the load and *b* is the sample's width. The expression $R = G$, given by equation 1, represents the stable crack propagation condition when $dG/da \leq dR/da$.

The stress intensity factor can be determined at any point of the $P \times \delta$-curve using the following relation:

$$K_I(\alpha_i) = \frac{P(\alpha_i)}{bw^{1/2}} \cdot y(\alpha_i), \qquad (2)$$

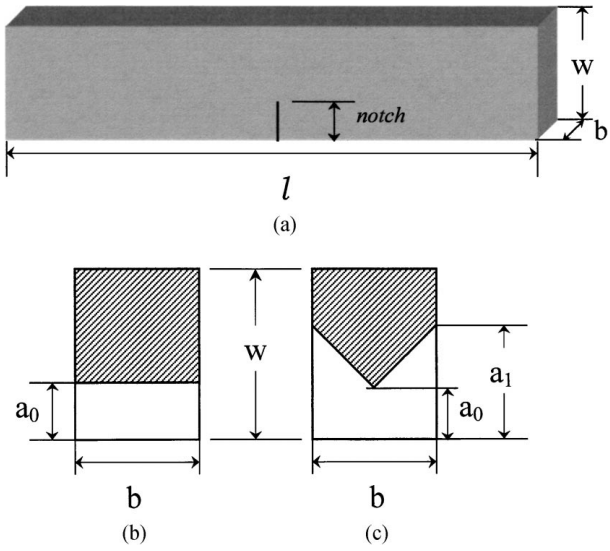

Figure 3 Sample dimensions. (a) View in perspective: l, length; b, width and w, height. (b) Cross-section of a straight-through notched sample. (c) Cross section of a Chevron notched sample, where a_1 is the height where the crack changes from Chevron to straight-through notch geometry during its propagation. The a_0 denotes the notch depth for both notches. The angle at the Chevron notch tip is 90°.

where α_i is the instantaneous relative crack length, given by a_i/w, $y(\alpha)$ is a geometrical factor depending on α and w corresponds to the sample's height. The $y(\alpha)$ function is chosen according to the test, notch and sample geometry. From Equations 1 and 2, it can be deduced that:

$$C(\alpha) - C(\alpha_0) = \frac{2}{bE}\int_{\alpha_0}^{\alpha} y^2(\alpha')\,d\alpha', \qquad (3)$$

where $C(\alpha_0)$ is the initial compliance of the notched sample with a relative notch depth equal to $\alpha_0 = a_0/w$. If $y(\alpha)$ does not present analytical integration, a numerical one can be applied based on the sum of the small rectangular areas, represented by:

$$C(\alpha) - C(\alpha_0) = \frac{2}{bE}\sum_j \left\{\left[\frac{(y(\alpha_j))^2 + (y(\alpha_{j-1}))^2}{2}\right] \cdot(\alpha_j - \alpha_{j-1})\right\}, \qquad (4)$$

where $(\alpha_j - \alpha_{j-1})$ assumes small values and defines the error of the integration. The integration is performed on the $(y(\alpha))^2$ function with limits ranging from α_0 to the requested α.

With the instantaneous values of α, $K_I(\alpha)$ can be calculated using equation 2 and, in turn, $R(\alpha)$, through Equation 1.

Following the mentioned above steps, this work presents the R-curve behavior of some alumina-mullite-zirconia composites with different amounts of zirconia and mullite inclusions. The R-curves obtained as a function of the different amounts of these inclusions is discussed, based on the toughening mechanisms. It is also verified that the R-curve shape is altered according to some test parameters. Moreover, it is shown that the $y(\alpha)$ function has a strong influence at the end of the R-curve in the region where the crack extends to the remaining 20% of its course.

TABLE II Composite formulation and estimated amounts of alumina, mullite and zirconia [12]

	Raw materials		Amounts of alumina, zirconia and mullite expected after the reaction sintering process[a]		
Composite designation	Al_2O_3 (wt-%)	$ZrSiO_4$ (wt-%)	Al_2O_3 (vol-%)	ZrO_2 (vol-%)	Mullite (vol-%)
0	100	0	100	0	0
1	95	5	88.5	2.7	8.8
2	90	10	78.2	5.3	16.5
3	85	15	67.7	7.9	24.4
4	80	20	57.5	10.3	32.2
5	75	25	47.6	12.7	39.7

[a]The percentages of each phase were calculated based on the chemical equation: $(3+x)\ Al_2O_3 + 2ZrSiO_4 \rightarrow xAl_2O_3 + 2ZrO_2 + 3Al_2O_3 \cdot 2SiO_2$

2. Experimental procedure

Alumina (A-16 SG*) and zircon (A-1000†) powders were used to produce the alumina-mullite-zirconia composites. The zircon powder was previously ball milled up to an average particle size of 2 μm (100% < 10 μm). Table II presents the five different composites produced, in which the amount of zircon ranged from 5 to 25 wt-%. The composition designated as "0" is pure alumina and was used as reference. Light ball milling followed by spray-drying was used to produce the alumina, zircon and water mixture. Bars of $62 \times 5 \times 6\,mm^3$ were produced by uniaxial compaction under 60 MPa pressure. Reaction sintering was carried out at 1650°C for 2 hours. The sintered samples were machined and parallel surfaces were obtained. Further information about the composites' processing steps, as well as their physical characterizations, can be found in Mazzei and Rodrigues [12].

To determine the R-curve, initially, the $P \times \delta$-curves under stable crack propagation condition were obtained. These curves were the result of flexural tests under three and four-point bending with straight-through and Chevron notched samples (Fig. 3b and c, respectively). Both types of notches were produced with a 150 μm thick diamond disc and a depth of $a_0/w = 0.35$.

The instantaneous crack length, a, was worked out through the $P \times \delta$-curves, by the change in the compliance, C, and the numerical integration given by Equation 4. The $K_I(\alpha)$ and $R(\alpha)$ values were evaluated using Equations 2 and 1, respectively, after introducing the E-value previously obtained by the three-point bending test [12]. All the calculations mentioned earlier were done using a software in the Visual Basic language developed by Zamprogno *et al.* [13]. All the mechanical tests were conducted in an MTS machine (810 series, MTS, Minneapolis, USA).

* ALCOA S/A, Poços de Caldas, MG, BR.
† NUCLEMON, Barra Funda, SP, BR.

The $y(\alpha)$ function used is given below:

$$y(\alpha) = \frac{(S_1 - S_2)}{w} \cdot \left[\frac{3\alpha^{1/2}}{2(1-\alpha)^{3/2}}\right] \cdot \left\{1.99 - 1.33\alpha - (3.49 - 0.68\alpha + 1.35\alpha^2) \cdot \left[\frac{\alpha(1-\alpha)}{(1+\alpha)^2}\right]\right\} \cdot \quad (5)$$

This equation can be applied for flexural tests under three or four-point bending configuration and samples with straight-through notch [14]. In Equation 5, S_1 is the lower span and S_2 is the distance between the centers of the upper rollers. In this work, $S_1 = 40$ mm flexural fixtures were used, while $S_2 = 20$ mm was used in the case of four-point bending. For the Chevron notched samples, the $y(\alpha)$ function given by equation 5 was corrected by a factor, considering the Chevron geometry [15]:

$$y(\alpha)_{\text{Chevron}} = y(\alpha) \cdot \left(\frac{\alpha_1 - \alpha_0}{\alpha - \alpha_0}\right)^{1/2} \cdot \quad (6)$$

In Equation 6, α_1 is the relative height (a_1/w) where the crack changes from Chevron to straight-through geometry during its propagation (see Fig. 3c). For $\alpha > \alpha_1$, $y(\alpha)_{\text{Chevron}}$ is identical to $y(\alpha)$ given by Equation 5.

In order to associate the R-curve shape with the toughening mechanisms, the fracture surfaces obtained under the stable crack propagation condition were observed with a scanning electron microscope (SEM, model 440, Leica Cambridge Steoreoscan, Cambridge, England).

As a standard reference for the R-curve, bars of $50 \times 3 \times 2$ mm^3 of commercial glass [estimated composition (wt-%): 72.1 SiO2, 13.6 NaO, 10.2 CaO, 2.6 MgO, 1.1 Al_2O_3 and 0.2 Fe_2O_3] were tested under three-point bending. An $a_0/w = 0.35$ Chevron notch was used for these experiments.

3. Results and discussion

$P \times \delta$-curves, under stable crack propagation, using straight-through notched samples, were only obtained for composites 3, 4 and 5. Chevron notched samples, on the other hand, allowed stable crack propagation under three and four-point bending for all composites. Fig. 4 presents some $P \times \delta$-curves obtained in this work.

The following analyses were carried out after R-curve evaluation:

i. changes in the R-curve as a function of the flexural test and notch geometries;

ii. influence of the $y(\alpha)$ function on the R-curve shape, especially at the region where $\alpha \geq 0.8$.;

iii. R-curve profile as a function of the amounts of zirconia and mullite inclusions.

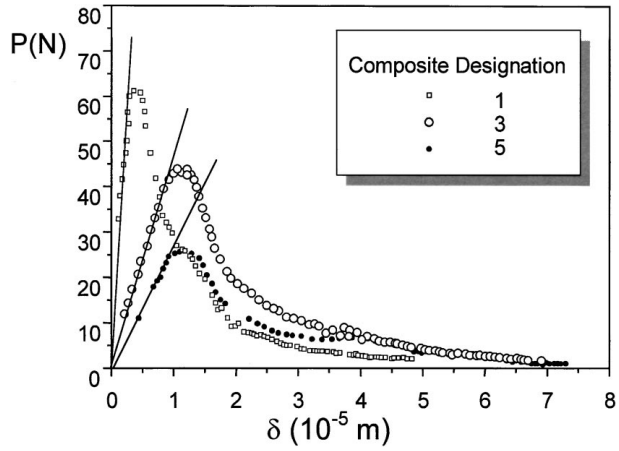

Figure 4 $P \times \delta$-curves for composites 1, 3 and 5 obtained with Chevron notched samples under three-point bending.

3.1. R-curve behavior as a function of the flexural test and notch geometry

To evaluate the test geometry, three and four-point bending configurations were considered, while for the notch geometry, the Chevron and straight-through were analyzed.

Fig. 5 shows the comparison among the R-curves obtained for three and four-point bending tests, using Chevron notched samples for composites 0, 1, 3 and 5. The $y(\alpha)_{\text{Chevron}}$ function given by Equation 6 was used to calculate the R-values.

The R-curves obtained from $P \times \delta$ curves under three and four-point bending tests show interesting features since the loading application location changes between these two configurations. For the three-point bending, the upper loading roller might generate an extra compressive field against the crack propagation path, although the results in Fig. 5 do not show this effect.

One can see, from Fig. 5, that the R-curves obtained from $P \times \delta$ curves under three-point bending, as well as those obtained from $P \times \delta$ curves under four-point bending, show a strong rise toward high values of α. Furthermore, one can also observe that the test geometry does not significantly affect the R-curve shape in the range of $\alpha_0 \leq \alpha \leq 0.8$. Therefore, considering these results and the fact that crack propagation stability is more easily attained under three-point bending, this arrangement was chosen for the overall composite characterization.

With respect to the notch geometry, a comparison among the R-curves obtained with Chevron and straight-through notches is shown in Fig. 6. The corresponding $y(\alpha)$ and $y(\alpha)_{\text{Chevron}}$ functions used for straight-through and Chevron notches are those given by Equations 5 and 6, respectively.

Fig. 6 clearly shows the difference between the R-curves obtained using samples with different notches. The curves associated to the straight-through notch showed a rising behavior right from the start. On the other hand, the curves corresponding to the Chevron notched samples presented an initial plateau. For both notch geometries, the R-curves presented an exaggerated increase at the end portion of the α scale. Selecting

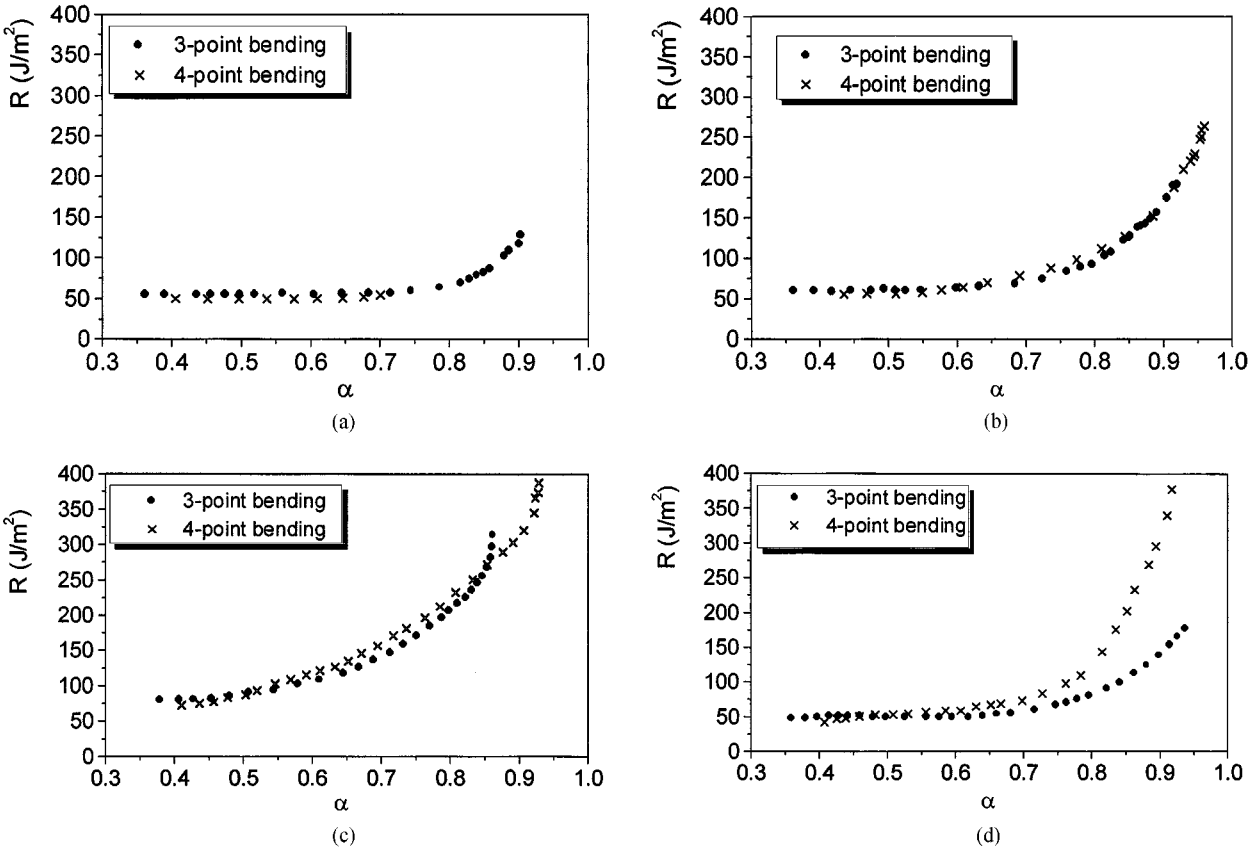

Figure 5 Average *R*-curves obtained under three and four-point bending tests for Chevron notched samples. (a) Pure alumina; (b) composite 1; (c) composite 3; and (d) composite 5.

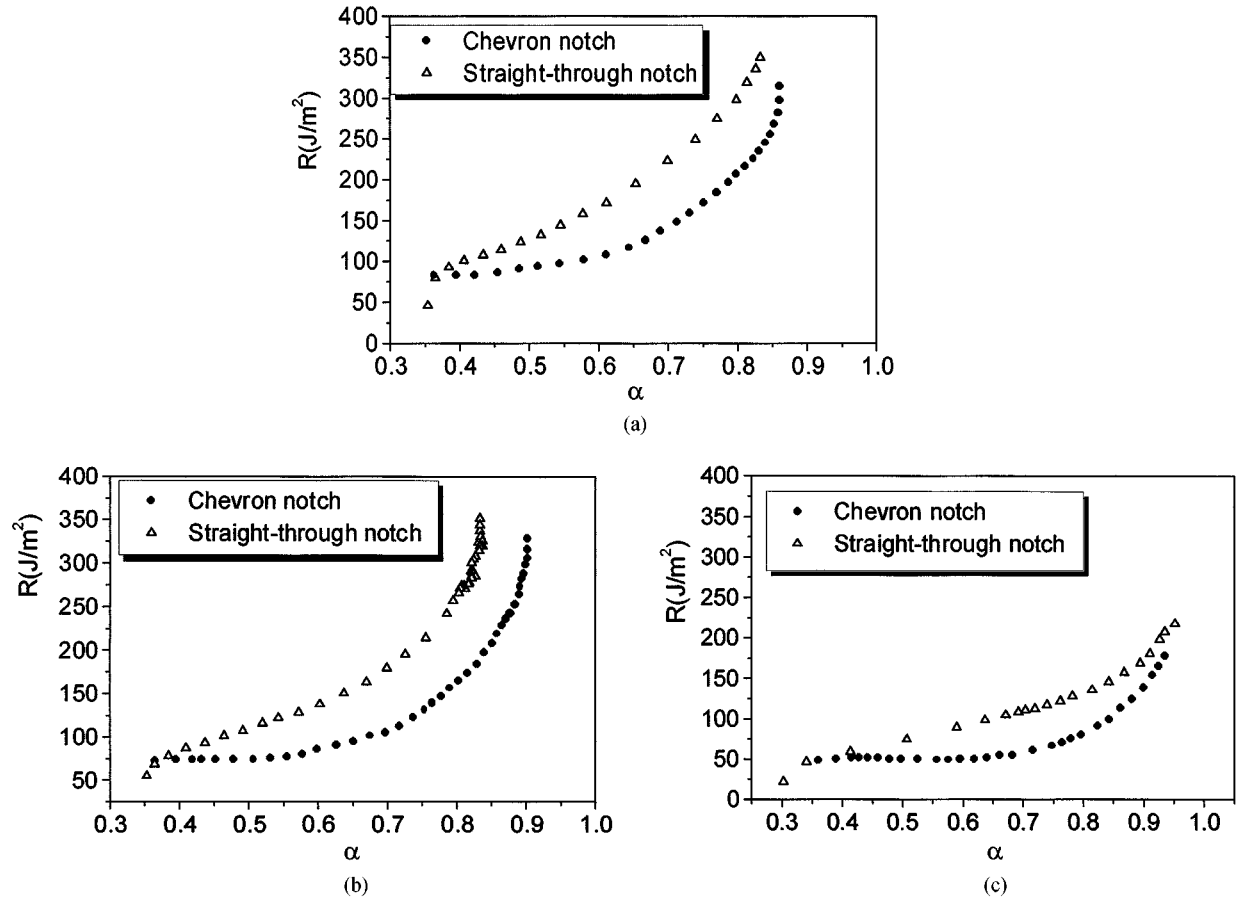

Figure 6 Average *R*-curves obtained under three-point bending test using Chevron and straight-through notched samples. (a) Composite 3; (b) composite 4; and (c) composite 5.

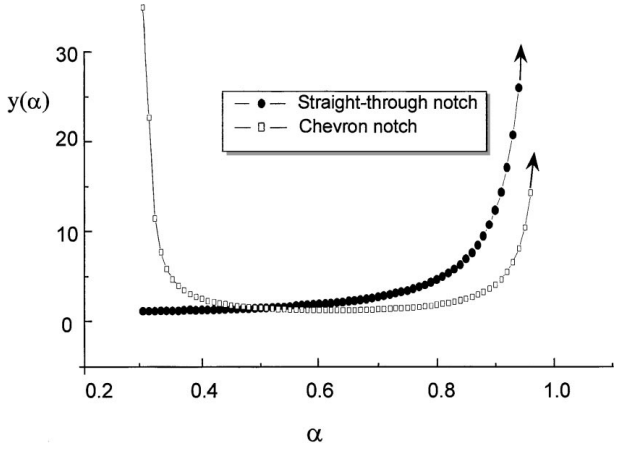

Figure 7 The shape of the $y(\alpha)$ functions used to calculate the R-values obtained from three-point bending test for straight-through and Chevron notched samples (Equations 5 and 6, respectively). The values used for α_0 and α_1 were 0.3 and 0.98, respectively.

one of these different behaviors is essential if association with possible toughening mechanism is sought.

3.2. R-curve behavior as a function of $y(\alpha)$

Equations 5 and 6 are plotted in Fig. 7. The $y(\alpha)_{\text{Chevron}}$ function presents a flatter behavior than the $y(\alpha)$ function for the straight-through notch in the interval $0.4 \leq \alpha \leq 0.9$. Therefore, it is assumed that the shape shown by the R-curve derives, in large part, from the $y(\alpha)$ function (see Fig. 6) and is not due solely to the toughening mechanisms.

Another relevant aspect related to the $y(\alpha)$ function for the Chevron notch is its influence on the R-curve shape for $\alpha \cong \alpha_0$. According to Fig. 8a, the R-curve obtained for Chevron notched samples presents high initial R-values. The same occurs for the $y(\alpha)$ function for the Chevron notch (see Fig. 7). This singularity at the beginning of the R-curve does not have any physical meaning considering the microstructure of the composites and the fact that the value of K_{IC} is finite. Therefore, this work used the following criteria to analyze the R-curves obtained from Chevron notched samples: the first value of R ($\alpha \cong \alpha_0$) was considered the one closest to the plateau of the curve, as exemplified in Fig. 8a. The problem inherent in this assumption lies in the difficulty of discovering the real R-value in regions where α is very close to α_0 (at the beginning of the R-curve). On the other hand, it is possible to define the beginning of the curve obtained with straight-through notched samples (see Fig. 8b), since the corresponding $y(\alpha)$ curve has no singularity for $\alpha = \alpha_0$ (see Fig. 7).

The high R-values for $\alpha \geq 0.8$ were also investigated. There are three possible reasons to explain this feature:

1) the strong rise of the R-curve could be the result of compressive fields at the crack tip, generated by the test geometry;
2) it could be a consequence of some microstructural aspect, such as grain interlocking between both fracture surfaces; or
3) it could be due to the $y(\alpha)$ function.

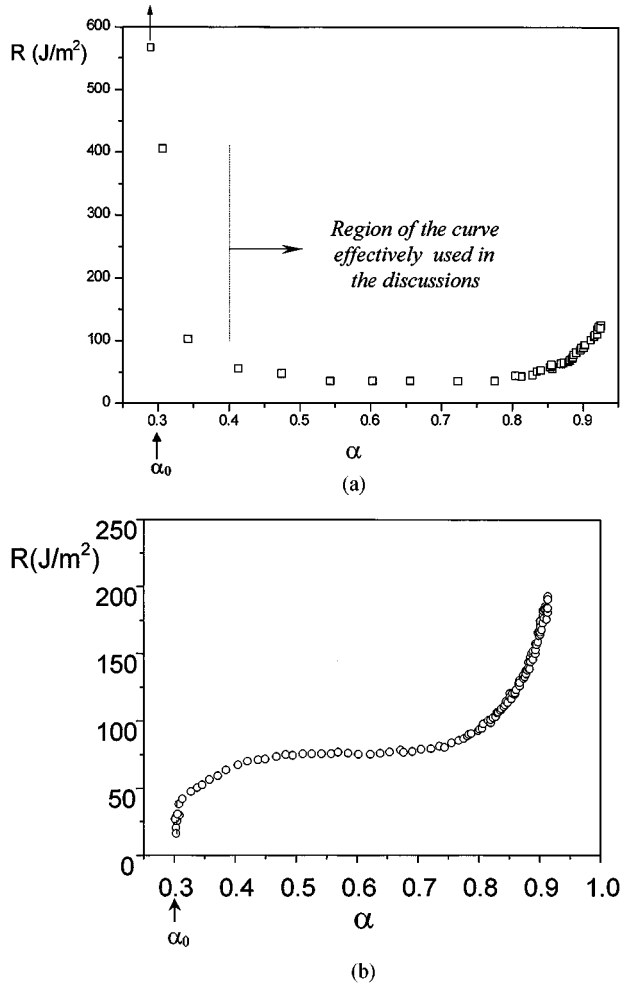

Figure 8 (a) R-curve obtained for pure alumina using a Chevron notched sample and three-point bending test. The R-value comes from the infinite when $\alpha \cong \alpha_0$ ($\alpha_0 = 0.3$, in this case). The horizontal arrow in this figure shows the part of the R-curve considered in the discussions. (b) R-curve obtained for composite 4 using three-point bending test and straight-through notched sample. In this curve, one can observe the initial rise of the R-values in the region where $\alpha \cong \alpha_0$.

Against the first supposition there is the fact that Fig. 5 shows either no difference among three and four-point configurations or the opposite tendency for $\alpha \geq 0.8$.

In order to investigate the second supposition, bars of a commercial glass were tested under the same conditions used for the composites. Fig. 9 shows that there is a strong rise in the R-values for $\alpha \geq 0.8$. It is a well known fact that commercial glass does not have any kind of toughening mechanism allowing such crack energy dissipation. Moreover, there are no grains for a possible interlocking process. Theoretically, this material must show a flat R-curve behavior in the $\alpha_0 \leq \alpha \leq 1.0$ range [16]. Hence, it might be concluded that a sharp artificial rise of the calculated values of R, considering $\alpha \geq 0.8$, also results from the $y(\alpha)$ function shape, as shown in Fig. 7.

3.3. R-curve behavior as a function of zirconia and mullite inclusions amounts

Fig. 10 shows the R-curves obtained for the Chevron notched composites 1 to 5 under three-point bending. The figure also presents the corresponding R-curve for

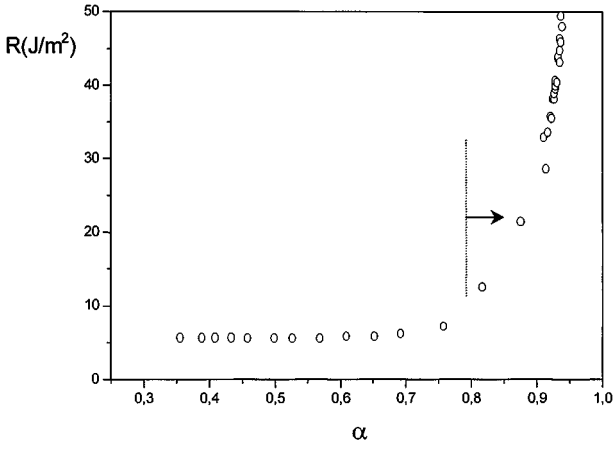

Figure 9 Average of the *R*-curves obtained for commercial glass using Chevron notched samples and three-point bending tests. A strong rise of the *R*-values in the region where $\alpha \geq 0.8$ can be observed.

pure alumina (composite designation "0"). Each resulting curve in Fig. 10 represents the average of 5 experiments obtained from different specimens with the same composition.

Concerning pure alumina, the *R*-curve was not flat for $\alpha \geq 0.8$. Considering that the microstructural analysis revealed an average grain size of 4 μm, a flat *R*-curve for $\alpha_0 \leq \alpha \leq 1.0$ was expected since the grains are rather too small to produce any friction or interlocking between the grains. Furthermore, this material did not suffer any microcracking during processing. A flat *R*-curve behavior for pure aluminas with grain size under 7 μm was observed in the literature [17].

As previously discussed, a strong rise of the *R*-values for $\alpha \geq 0.8$, as well as the *R*-curve shape, are affected by the $y(\alpha)$ function. Thus, in order to examine the variation of the *R*-curve behavior as a function of the amount of zirconia and mullite inclusions, the *R*-values obtained for pure alumina were deducted from the *R*-values obtained for each composite. This subtraction might suppress the influence of the $y(\alpha)$ function, generating *R*-curves where only the toughening mechanisms present in the composites prevail. Fig. 11 shows the resulting *R*-curves.

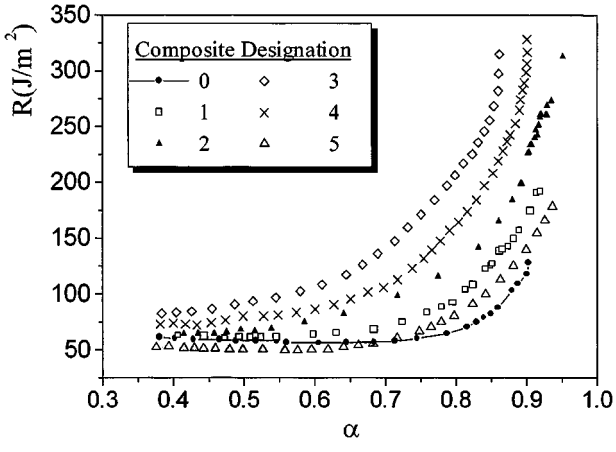

Figure 10 Changes in the *R*-curve shape due to the initial amount of zircon (the figure shows the composite designation according to Table II). Three-point bending and Chevron notched samples were used in all of these tests.

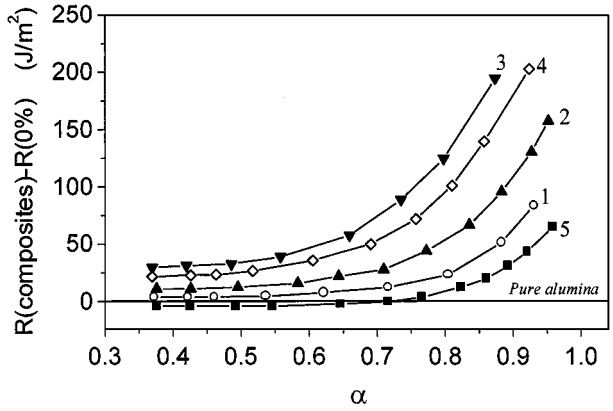

Figure 11 *R*-curves obtained substracting the *R*-values of pure alumina from the *R*- curve of each composite. The tests were conducted with Chevron notched samples under three-point bending. The numbers associated to the curves indicate the composite designation (Table II).

TABLE III Mechanical properties and the linear thermal expansion coefficient (α_{th}) for the composites [12]

Composite designation	σ_f (MPa)	K_{IC}^a (MPa · m$^{1/2}$)	E (GPa)	α_{th} ($\times 10^{-6}$ °C^{-1})
0	332 ± 25	5.34 ± 0.28	378 ± 42	8.77
1	295 ± 20	5.25 ± 0.14	296 ± 10	8.39
2	295 ± 37	5.41 ± 0.31	295 ± 12	8.33
3	317 ± 35	5.57 ± 0.03	255 ± 44	7.44
4	204 ± 65	3.54 ± 0.22	173 ± 6	7.44
5	118 ± 20	3.36 ± 0.14	178 ± 30	7.39

[a]A straight-through notch thickness of 200 μm was used.

Fig. 11 shows a slight increase in the *R*-curve values for composites 1 and 2 compared to that obtained for pure alumina. The initial *R*-values for these curves are quite similar and an increase of the *R*-values with α is observed.

The highest toughening effect was verified for composite 3, which was produced with 15 wt-% of zircon. The improvements observed can be divided into two aspects:

1) The initial level of the *R*-curve is higher, indicating that the crack propagation initiation energy increased as a consequence of toughening mechanisms that operate at the crack tip. One of these mechanisms may be crack deflection caused by the zirconia inclusions. Moreover, the zirconia inclusions can display reinforcement components since their phase transformation can build up compressive stresses in the matrix and also promote decreases in the average grain size of the alumina phase (comparing pure alumina with composite 3, a reduction of 20% in the average grain size was observed). The proof of these statements are the higher values of σ_f and K_{IC} verified for composite 3 (see Table III) [12];

2) There is a considerable slope increase in the *R*-curve, indicating toughening mechanisms which the process zone continuously develops with increased crack length. These mechanisms, among them crack branching, are generated by the zirconia and mullite inclusions.

For composites 4 and 5, a degradation of the *R*-curve behavior is observed in relation to that obtained for composite 3. It is worth noting that, for composite 5, the initial plateau of the *R*-curve is lower than the one for pure alumina (see Fig. 11). Observing Table III, the degradation of all mechanical properties is clear for composites 4 and 5. Some explanations for these changes were given in Mazzei *et al.* [12, 18]. Another interesting point in Fig. 11 and Table III is to verify the matching between the initial *R*-value and K_{IC}.

The changes in the *R*-curves can be attributed to the toughening mechanisms produced by the zirconia and

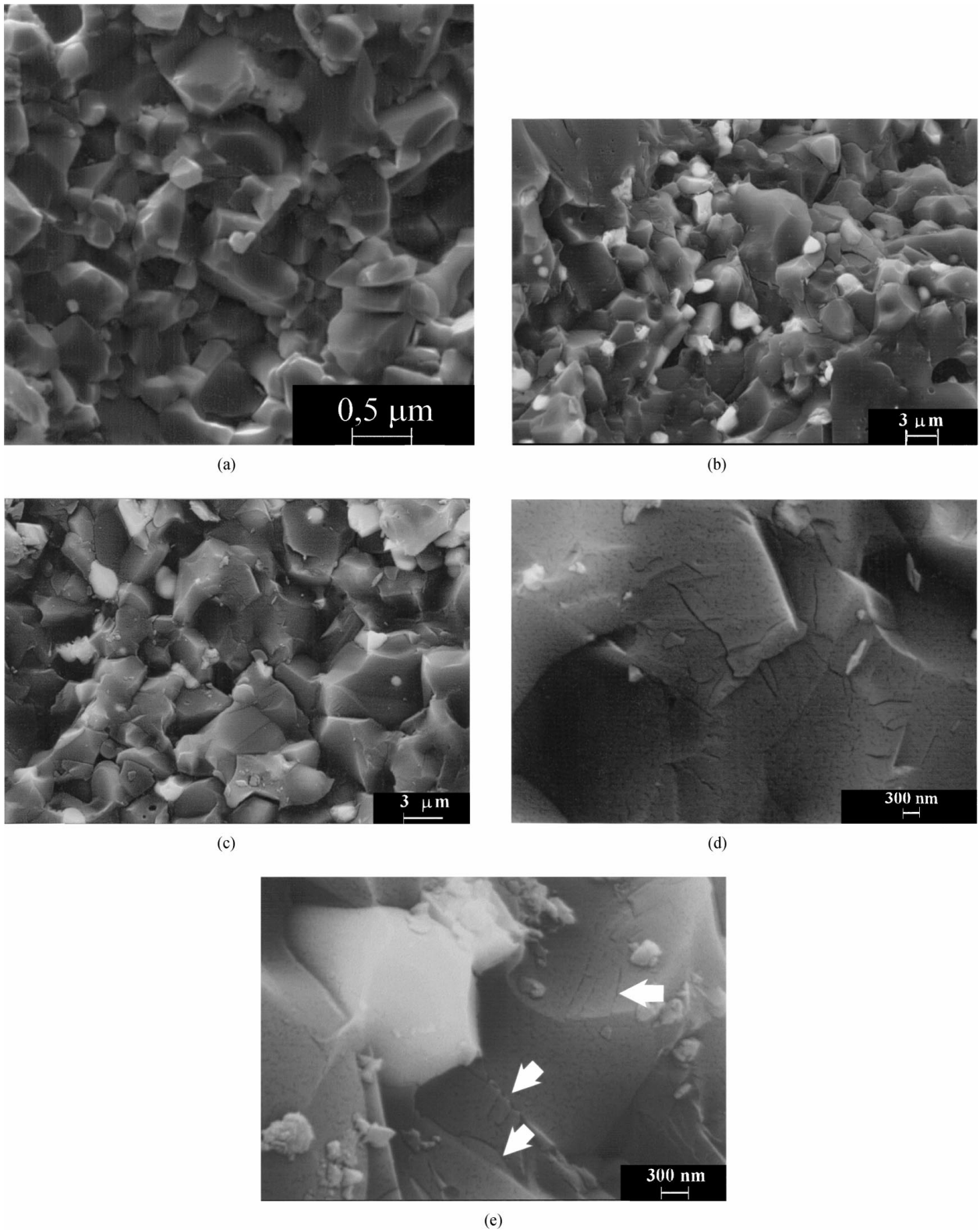

Figure 12 Micrographs of the fracture surfaces obtained under a stable crack propagation condition. (a) Pure alumina; (b) composite 2; (c) and (d) composite 3 and (e) composite 5. In micrographs (b) and (c), microcracks generated as a consequence of crack branching and grain detachment can be seen. In micrograph (d), microcracks produced as a consequence of the tetragonal-monoclinic phase transformation of the zirconia during sintering cooling, in a region that was probably occupied by a zirconia inclusion can be seen. In (e), the microcracks produced by the phase transformation surround a zirconia particle.

mullite inclusions in the alumina matrix. The investigation of these mechanisms is based on the SEM observation of the fracture surfaces obtained under a stable crack propagation condition. Fig. 12 shows a set of micrographs of the most representative fracture surfaces for pure alumina and composites 2, 3 and 5.

Regarding these micrographs, it is worth pointing out that:

1) Intergranular fractures at the alumina-alumina and alumina-zirconia interfaces were observed;

2) Microcracks were verified on the fracture surface, which could be an indication of crack branching;

3) Fine radial microcracking in the alumina matrix was observed in regions that were probably occupied by zirconia inclusions (see Fig. 12d), as well as in areas close to these inclusions (see Fig. 12e). It was assumed that these smaller microcracks were generated by the tetragonal-monoclinic phase transformation of the zirconia that occurred during sintering cooling. Moreover, X-ray diffraction characterization of the composites revealed that the zirconia appears mainly as the monoclinic phase [12]. Lastly, these microcracks could also be generated during the fracture process, but this possibility was rejected since such microcracks were not found on the pure alumina fracture surface.

Based on the above, it was concluded that the main toughening mechanism operating in the composites was crack branching. There were also contributions of the zirconia-zirconia interface detachment and some bridging caused by casual mullite inclusions grown in a needle-like shape, leading to the inference that the changes in R-curve values and shapes are a function of the amount of zirconia and mullite inclusions.

For composites 1 and 2, the ability of the microstructure to branch out the crack is very slight, since the concentration of zirconia and mullite inclusions is low. The best performance is achieved for composite 3. Increased amounts of zirconia and mullite inclusions improve the R-curve behavior of composites 1 to 3 compared to that obtained for pure alumina. Further additions of zircon prior to reaction sintering (composites 4 and 5) increase porosity (generated by the dissociative reaction of the zircon) and pore coalescence [12, 18], which in turn, causes degradation in the R-curve behavior as a consequence of matrix weakening.

4. Conclusions

Changes in the R-curve profile due to notch geometry (Chevron or straight-through notches) were observed and are attributed to the influence of the $y(\alpha)$ function. Considering the interval of $\alpha_0 \leq \alpha \leq 0.9$, the $y(\alpha) \times \alpha$ plots presented a flatter curve for Chevron notch and a rising behavior for the straight-through geometry, producing a similar influence on the shape of the calculated R-curves. Moreover, it was discovered that the strong rise in the values of R to $\alpha \geq 0.8$ is also a direct consequence of the $y(\alpha)$ function shape.

In this sense, the variation of the R-curve as a function of the amounts of zirconia and mullite inclusions was verified by subtracting the R-curve obtained for pure alumina from the one obtained for each composite resulting from reaction sintering. The highest energy consumption composite was obtained with 15 wt-% of zircon mixed with alumina. Additional increases in the zircon amount resulted in pore coalescence and also caused increased microcracking in the matrix. Pore coalescence was caused by the additional porosity that occurred owing to the dissociative reaction of zircon. Increased porosity and microcracking of the composites containing 20 and 25 wt-% of zircon attenuated the R-values.

The composite produced with 15 wt-% of zircon presented a steady increase in the R-curve profile as a result of the active toughening mechanisms. In this composite, the initial R-value was higher compared to the pure alumina one, indicating greater starting propagation resistance, and its corresponding R-curve was steeper than the others.

Lastly, the main toughening mechanism identified in the alumina-mullite-zirconia composites was crack branching, due to the microcracks generated in the alumina matrix by the resulting zirconia inclusions. Tetragonal-monoclinic phase transformation occurring during the sintering cooling was the principal cause of microcracking.

Acknowledgements

The authors would like to thank ALCOA ALUMINIO S/A for supplying some of the raw materials and FAPESP, CAPES and CNPq for their financial support.

References

1. E. D. ZANOTTO and A. R. MIGLIORE, *Cerâmica* **37** (1991) 247.
2. A. G. EVANS and R. M. CANNON, *Acta. Metal.* **34** (1986) 5.
3. E. C. SUBBARAO in "Science and Technology of Zirconia—Advances in Ceramics", Vol. 3, edited by A. H. Heuer and L. W. Hobbs (Cleveland, Ohio, 1981) p. 1–24.
4. F. CAMBIER, C. BAUDIN, P. PILATI and A. LERICH, *Brit. Cer. Trans. Journ.* **83** (1984) 196.
5. S. PROCHASKA, J. S. WALLACE and N. CLAUSSEN, *Jour. of the Amer. Ceram. Soc.* **66**[N-8] c125–7.
6. M. SAKAI and R. C. BRADT, *Journ. of Ceram. Soc. Jap. Int.* **96** (1988) 779.
7. Standard Test Method for Plane Strain Fracture Toughness of Metallic Materials ASTM E-399 (1981).
8. P. S. SHAH and C. OUYANG, *Journ. Eng. Mat. and Tech.* **115** (1993) 300.
9. Rilem Draft Recommendations, TC 89-FMT, *Materials and Structures* **23** (1990) 457.
10. H. HÜBNER and W. JILLEK, *Journ. of Mat. Sci.* **12** (1977) 117.
11. M. F. A. MAGON, J. A. RODRIGUES and V. C. PANDOLFELLI, Proceedings of the 39th Congresso Brasileiro de Cerâmicas, Águas de Lindóia, SP, Brazil (Associação Brasileira de Cerâmicas, 1995). Vol I, p. 478.
12. A. C. A. MAZZEI and J. A. RODRIGUES, *J. Mater. Sci.* **35** (2000) 2807.
13. J. A. RODRIGUES, E. R. ZAMPROGNO and V. C. PANDOLFELLI, Proceedings of the 41st Congresso Brasileiro e Cerâmicas, São Paulo—SP, Brazil, junho de 1997 (Associação Brasileira de Cerâmica, 1997) Vol II, p. 510.

14. J. E. SRAWLEY and B. GROSS, ASTM STP601 (American Ceramic Society for Testing and Materials, 1976) p. 559.
15. L. P. POOK. *Int. J. Fract. Mechanics.* **8** (1972) 103.
16. F. W. KLEINLEIN and H. HUBNER, *Fracture* **3** (1977) 19.
17. R. W. STEINBRECH, "*R*-Curve Behavior of Ceramics" in "Fracture Mechanics of Ceramics", Vol. 9 edited by R. C. Bradt, D. P. H. Hasselman, D. Munz and M. Sakai, (Plenum Press, NY, 1992) p. 187.
18. A. C. A. MAZZEI, J. A. RODRIGUES and V. C. PANDOLFELLI, Proceedings of the 41st Congresso Brasileiro e Cerâmicas, São Paulo—SP, Brazil, junho de 1997 (Associação Brasileira de Cerâmica, 1997) Vol. I, p. 237.

Received 1 September 1998
and accepted 15 July 1999